The Astronomical Journal, 170:190 (15pp), 2025 September https://doi.org/10.3847/1538-3881/adf641

OGLE-2014-BLG-1760: A Jupiter–Sun Analogue Residing in the Galactic Bulge

Natalia E. Rektsini[1,2], Clément Ranc[2], Naoki Koshimoto[3], Jean-Philippe Beaulieu[1,2], David P. Bennett[4,5], Andrew A. Cole[1], Sean K. Terry[4,5], Aparna Bhattacharya[4,5], Étienne Bachelet[6], Ian A. Bond[7], Andrzej Udalski[8], Joshua W. Blackman[9], Aikaterini Vandorou[4,5], Thomas J. Plunkett[1], and Jean-Baptiste Marquette[2,10]
[1] School of Natural Sciences, University of Tasmania, Private Bag 37 Hobart, Tasmania, 7001, Australia; efstathia.rektsini@utas.edu.au
[2] Sorbonne Université, CNRS, Institut d'Astrophysique de Paris, IAP, F-75014, Paris, France
[3] Department of Earth and Space Science, Graduate School of Science, Osaka University, Toyonaka, Osaka 560-0043, Japan
[4] Code 667, NASA Goddard Space Flight Center, Greenbelt, MD 20771, USA
[5] Department of Astronomy, University of Maryland, College Park, MD 20742, USA
[6] IPAC, Mail Code 100-22, Caltech, 1200 East California Boulevard, Pasadena, CA 91125, USA
[7] Institute of Natural and Mathematical Sciences, Massey University, Auckland 0745, New Zealand
[8] Astronomical Observatory, University of Warsaw, Aleja Ujazdowskie 4, 00-478 Warszawa, Poland
[9] Physikalisches Institut, University of Bern, Gesellschaftsstrasse 6, 3012 Bern, Switzerland
[10] Laboratoire d'astrophysique de Bordeaux, Univ. Bordeaux, CNRS, B18N, alle Geoffroy Saint-Hilaire, 33615 Pessac, France
Received 2024 October 13; revised 2025 July 5; accepted 2025 July 29; published 2025 September 1

Abstract

We present the analysis of OGLE-2014-BLG-1760, a planetary system in the galactic bulge. We combine Keck Adaptive Optics follow-up observations in *K*-band with re-reduced light-curve data to confirm the source and lens star identifications and stellar types. The re-reduced Microlensing Observations in Astrophysics data set had an important impact on the light-curve model. We find the Einstein ring crossing time of the event to be ∼2.5 days shorter than previous fits, which increases the planetary mass-ratio and decreases the source angular size by a factor of 0.25. Our OSIRIS images obtained 6 yr after the peak of the event show a source-lens separation of 54.20 ± 0.23 mas, which leads to a relative proper motion of $\mu_{\rm rel} = 9.14 \pm 0.05$ mas yr^{-1} and is larger than the previous light-curve-only models. Our analysis shows that the event consists of a Jupiter-mass planet of $M_{\rm p} = 0.931 \pm 0.117\ M_{\rm Jup}$ orbiting a K-dwarf star of $M_* = 0.803 \pm 0.097\ M_\odot$ with a *K*-magnitude of $K_{\rm L} = 18.30 \pm 0.05$, located in the galactic bulge or bar. We also attempt to constrain the source properties using the source angular size θ_* and *K*-magnitude. Our results favor the scenario of the source being a younger star in the galactic disk, behind the galactic bulge, but future multicolor observations are needed to constrain the source and thus the lens properties.

Unified Astronomy Thesaurus concepts: Gravitational microlensing (672); Exoplanets (498); Galactic bulge (2041); Adaptive optics (2281)

1. Introduction

Gravitational microlensing is a highly specialized technique to discover exoplanetary systems. More than 200 exoplanets have been detected via this technique since the idea that observations toward the Galactic bulge can lead to exoplanet detections (S. Mao & B. Paczynski 1991). Contrary to most planet detection methods, microlensing is independent of the host star mass and brightness. This allows us to detect planetary companions orbiting any type of massive object, whether stellar, substellar, or a compact remnant, in the Milky Way (B. S. Gaudi 2012). A unique opportunity given by microlensing is to be able to probe the populations of planets in the far disk and the bulge of the Galaxy, along the line of sight to the Galactic bulge. This can provide new insights about planetary system formation theory as a function of metallicity and environment.

Observing and then modeling the light curve of a microlensing event will provide accurate mass ratios between the star and its planet, and its projected separation in units of the angular Einstein ring radius. To learn about the physics of planetary systems, it is important to know with accuracy the physical parameters, mass, and distance of the host star and its planetary companion. Often, these physical parameters are derived from Bayesian analysis with a Galactic model, which can lead to typical uncertainties of 50% or more. In addition, this method can be insufficient for resolving degenerate or ambiguous models (A. Gould et al. 2006; J. Y. Choi et al. 2012; J. C. Yee et al. 2021). This means that we need to seek additional sources of information to constrain the physical parameters of the system.

Once such constraint comes from the change of alignment between the observer, the lens, and the source because of the Earth's orbit, leading to deformation of the light curve due to parallax effects. Measuring the microlensing parallax can lead to a strong constraint for the mass and distance of the lens. Unfortunately, this requires events to have quite long timescales of a few months, which is not always the case. A second approach is to use the angular size of the source. If the source transits the caustic, we are able to calculate an estimate of the Einstein ring radius, which can be translated into a mass–distance relation for the lens. Note that from the light curve alone, we only measure the source size and in most cases this measurement provides only a weak constraint for the Einstein ring radius.

A third route is to reobserve the microlensing system in the decade that follows the source-lens alignment using high-angular resolution techniques. Previous works (V. Batista et al. 2015; D. P. Bennett et al. 2015) have shown that using 10 m class telescopes equipped with adaptive optics, and/or

the Hubble Space Telescope can help us resolve the source and lens. This provides a constraint on the flux of the lens and allows us to measure the amplitude and direction of the source-lens relative proper motion with high precision. Measuring the relative proper motion also places a strong constraint on the angular Einstein ring radius and the microlensing parallax. This means that it is possible to combine three different mass and distance constraints on the lens, which can often lead to mass measurements of up to ∼10% precision (A. Bhattacharya et al. 2018; N. E. Rektsini et al. 2024).

Moreover, using KECK and/or HST high-angular resolution observations is part of the preparation strategies for the Nancy Grace Roman Space Telescope. Roman is one of the first space missions to carry a microlensing survey (Roman Galactic Bulge Time Domain Survey, B. S. Gaudi 2024). The survey is expected to discover more than 1400 bound planets (M. T. Penny et al. 2019) and on the order of a thousand unbound planets (S. A. Johnson et al. 2020; T. Sumi et al. 2023) via the microlensing technique. To maximize the number of planet detections with precise mass and distance measurements during the five year survey, Roman will conduct high-angular resolution follow-up observations regularly on the events previously discovered, aiming to eventually obtain images of the source and lens stars resolved and thus deduce accurate measurements of the physical parameters of the detected planetary systems. Several studies investigating the systematics and best approach to the analyses have already been completed (N. Koshimoto et al. 2017a; D. P. Bennett et al. 2020; A. Vandorou et al. 2020; J. W. Blackman et al. 2021; S. K. Terry et al. 2021, 2022; A. Bhattacharya et al. 2023), covering a large variety of microlensing events, a very important task to do before the start of the survey.

Here, we revisit the microlensing event OGLE-2014-BLG-1760, one of the most distant planetary systems discovered to date. In the discovery paper, A. Bhattacharya et al. (2016) show that this system is most likely to be a gas giant planet orbiting a G-, K-, or M-dwarf star near the Galactic bulge; this is conditional on the source star being located either close to the Galactic bulge or further away in the Galactic disk. We use Keck adaptive optics observations of the source and lens 5.94 yr following the event in order to constrain the source-lens relative proper motion and flux ratio, and finally deduce the precise mass and distance of the lens as well as the source color. We confirm that the planetary system is a cold Jupiter analog in the Galactic bulge.

This paper is organized as follows. Section 2 describes the microlensing event OGLE-2014-BLG-1760 and the conclusions drawn in the original detection paper. Section 3 presents our Keck high-angular resolution follow-up observations and their analysis. In Sections 3.2–3.4, we describe our point-spread function (PSF) fitting procedure, fitting the source and lens and measuring their separation and flux ratio. In Section 4, we present a new analysis of the light-curve model with and without the Keck constraints and in Section 5 we show our results for the planetary system. In Section 6, we study the source properties and finally in Section 7 we summarize our analysis and discuss our conclusions.

2. OGLE-2014-BLG-1760: The Event

The event was first announced as OGLE-2014-BLG-1760 by the Optical Gravitational Lensing Experiment (OGLE) Early Warning System (A. Udalski et al. 1994, 2004) on 2014 August 22. The Microlensing Observations in Astrophysics (MOA) collaboration (I. Bond et al. 2001) announced the event as MOA-2014-BLG-547 on 2014 August 31. The light curve, including a planetary cusp feature (Figure 2 from A. Bhattacharya et al. 2016), was well-covered by the microlensing follow-up groups RoboNet (Y. Tsapras et al. 2009) and μFUN (A. Gould et al. 2010b). Observations from RoboNet were conducted with 1 m robotic telescopes at Sutherland, South Africa and at Siding Spring, Australia in the Sloan i band. Observations from the μFUN group were made with the 1.3 m SMARTS CTIO telescope in I, V, and H bands but they were not used for the light-curve analysis. In this work, we decided not to use μFUN because their contribution does not affect the outcome of this study. The equatorial coordinates of the event are R.A. $= 17^{\rm h}57^{\rm m}38\overset{\rm s}{.}16$, decl. $=-28^{\circ}57'43\overset{''}{.}37$ (J2000.0) and the Galactic coordinates are $l = 1\overset{\circ}{.}3186$, $b = -2\overset{\circ}{.}2746$.

The event was first analyzed by A. Bhattacharya et al. (2016). The light curve is very well sampled in I and R bands but has only three V band observations by OGLE: two at the beginning and one at the end of the significantly magnified period. This leads to a color measurement of $(V-I)_{\rm OGLE,measured} = 1.45$, with a fairly large uncertainty of ±0.11. A. Bhattacharya et al. (2016) also used the MOA R-band observations to calculate the $(V-I)$ source color using the well constrained $R_{\rm MOA} - I$ color (A. Gould et al. 2010a). This gives them $(V-I)_{\rm MOA-OGLE,fitted} = 1.52 \pm 0.11$. Finally, they combine the two methods and obtain a source color of $(V-I)_{\rm adopted} = 1.48 \pm 0.08$.

In A. Bhattacharya et al. (2016), the extinction toward this direction, as in D. P. Bennett et al. (2014), is calculated by using the centroid of the red clump in the color–magnitude diagram as a standard crayon. In the OGLE-III catalog, this is found to be $(V-I, I)_{\rm RC} = (2.20, 15.84)$. Following T. Bensby et al. (2011) and D. M. Nataf et al. (2013), they adopted the dereddened red clump centroid as $(V-I, I)_{\rm RC} = (1.06, 14.39)$, which gives them the extinction to the source star residing inside the Galactic bulge to be $(E(V-I), A_I)_{\rm RC} = (1.14, 1.45)$, which gives the intrinsic source color and magnitude of $(V-I, I)_{\rm S,0} = (0.34 \pm 0.08, 17.62 \pm 0.14)$.

The event has a quite short timescale of around 16 days, with a very faint and highly blended source star. The magnification is mostly defined by the MOA-R data since they were the only group to record the caustic cusp passage. This makes the V band and the $(V-I)$ source color highly unreliable. The rather blue color of the source star that was estimated in A. Bhattacharya et al. (2016) led the authors to two different scenarios: the source may be a main-sequence star in the Galactic bulge, or a more luminous and bluer star in the far Galactic disk, behind the bulge. There are very few stars with such blue $(V-I)$ color in the bulge but the authors argue that since the stellar density of the disk is much lower than that of the bulge, the source star is more likely to be located in the bulge rather than beyond. This impacts on the interpretation of the distance and mass of the lens, and suggests that high-angular resolution follow-up is needed to further understand the nature of the planetary system.

3. Keck Adaptive Optics Follow-up

We observed OGLE-2014-BLG-1760 on 2020 August 9 in $K_{\rm p}$ band, using the OSIRIS imager on the Keck I telescope, 6 yr after the microlensing event. The images for this observational epoch can be found at B. Berriman (2024). A. Bhattacharya et al. (2016) estimated a geocentric source-lens

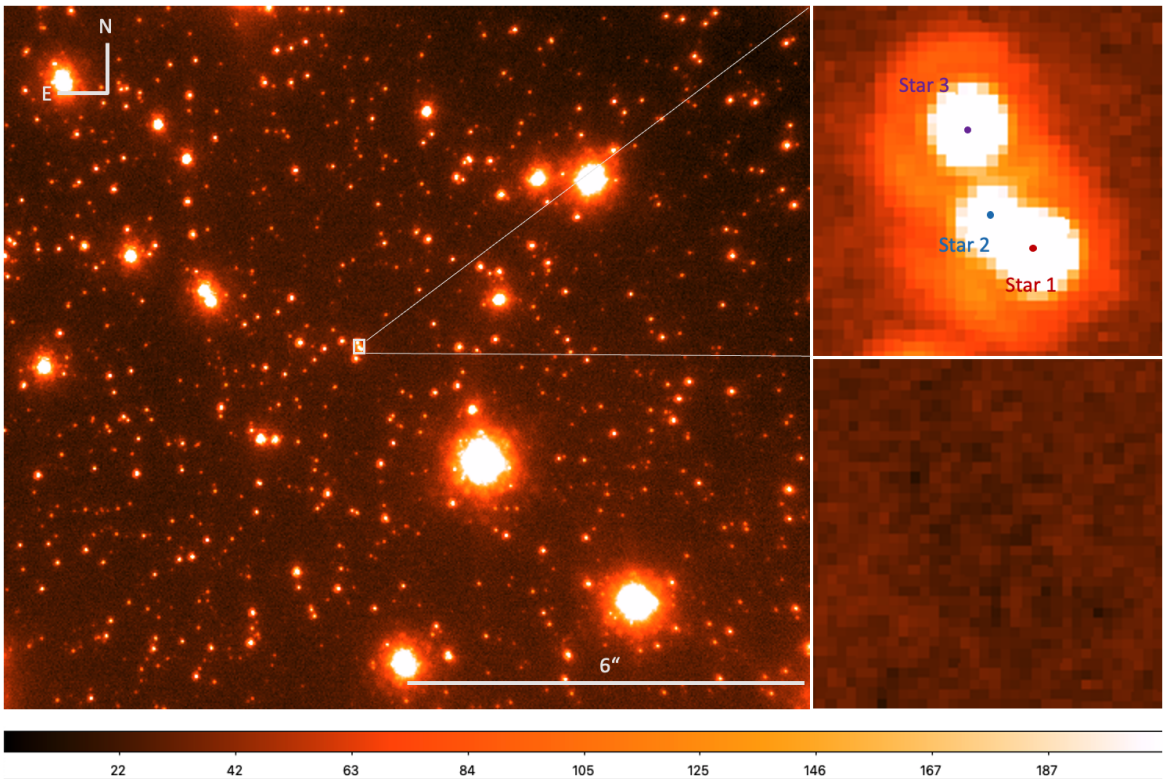

Figure 1. Left panel: Jackknife stack of 20 science frames of the 2020 August Keck OSIRIS K_p band follow-up observation. Upper right panel: Close-up ($0\farcs38 \times 0\farcs38$) frame of the source (star 1), the lens (star 2), and the third star (star 3), which is unrelated to the event. Lower right panel: Close-up ($0\farcs38 \times 0\farcs38$) of the three-star PSF fit residual using DAOPHOT.

relative proper motion of $\mu_{\rm rel,geo} = 6.55 \pm 1.12$ mas yr^{-1}, so we expected a source-lens separation comparable to the OSIRIS image resolution. The pixel scale of the OSIRIS camera is 9.96 mas pixel^{-1}. The images that we obtained had an average PSF FWHM of 54 mas and showed a clear resolution of the source and lens.

3.1. Analysis of the Keck Images

We obtained 20 science images, 10 dark, 20 flat field, and 10 sky frames. We used the KAI[11] (Keck AO Imaging) data reduction pipeline (J. R. Lu et al. 2021) to correct for geometric distortion and instrumental signatures of the OSIRIS camera, differential atmospheric refraction, and cosmic ray masking and produce a coadded science frame as shown in Figure 1.

3.1.1. Precise Position of the Source Star

Inspection of the Keck image revealed four stars close to the expected position of the source. (I.B.) identified the event's position by comparing the MOA star field with our OSIRIS stacked frame and found the expected position of the target to be close to star 1, as shown in Figure 1. In order to double-check the target identification, we also use the OGLE-IV catalog. (A.U.) linearly transformed coordinates of stars from the OGLE survey to the OSIRIS image, with residuals being at most at the 20–30 mas (2–3 OSIRIS pixels). Then, he recalculated the centroid of OGLE-2014-BLG-1760 based on 10 subtracted images taken at maximum magnification and transferred its position to the OSIRIS grid. The transformed centroid is located in the center of star 1. The accuracy of the centroid is ≈1 OSIRIS pixel (0.03 OGLE-IV pixel), so it can be neglected compared to the transformation accuracy. The latter is about 2–3 OSIRIS pixels. In combination with the expected source magnitude in K band from the light-curve analysis, we conclude that the centroid of the magnified source is conclusively identified with star 1 and not the fainter northeast companion some 5.4 pixels away (labeled star 2 in Figure 1).

3.1.2. Photometric Calibration of the Keck Images

We use standard techniques (e.g., J.-P. Beaulieu et al. 2016, 2018) to calibrate the OSIRIS stacked image. We calibrated against 2MASS K-band magnitudes from the VVV survey (D. Minniti et al. 2010). Thirteen isolated stars are common to VVV and OSIRIS. We estimated the uncertainty in our calibration to be 3%. We performed aperture photometry on the Keck OSIRIS frame, and measured the combined flux of star 1 and star 2 to be $K_{\rm S+L} = 16.92 \pm 0.06$.

3.1.3. Preparing the Keck Images for Jackknife Approach

We also used the jackknife routine as in previous studies (A. Bhattacharya et al. 2021; S. K. Terry et al. 2021) to produce a set of 20 images of 19 science coadded frames each, in order to obtain a distribution of the quality of the science frames we are using. This is important for quantifying the Strehl ratio and PSF FWHM uncertainties caused by atmospheric turbulence for each scientific frame. The PSF of each stacked frame of N−1 science images produced an average FWHM of 54 ± 0.2 mas, proving the good quality of all the science frames used. Finally, to measure the source and lens

[11] doi:10.5281/zenodo.6677744

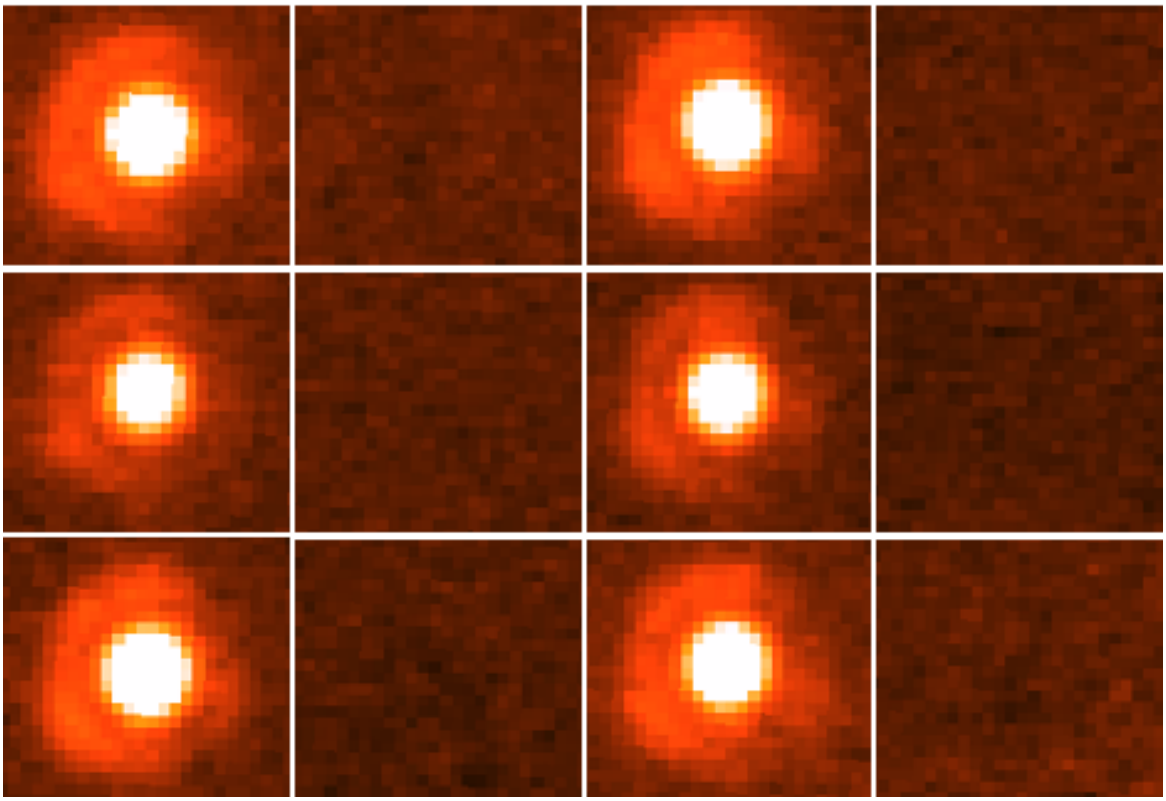

Figure 2. Close-up ($0\farcs2 \times 0\farcs2$) frames of the six stars used to construct the PSF model (right) and their residuals, after profile-fitting photometry subtraction (left).

precise positions and magnitudes, we perform PSF-fitting photometry on each of the 20 stacked science frames. We use DAOPHOT (P. B. Stetson 1987) to model the sky background, obtain initial magnitude estimates by aperture photometry, and finally construct an appropriate PSF model.

3.2. PSF Model

We began by running the standard DAOPHOT FIND and PHOT routines to fit the sky background and estimate instrumental magnitudes for each star. We restricted the search for good PSF stars to those with instrumental magnitude no more than 0.6 mag fainter than star 1. In addition, we chose to search only within a radius of 400 pixels around the target to ensure that all chosen stars will have the same PSF and also to eliminate those that are too close to the image edges. We found 47 stars that match the magnitude and distance criteria. We identified the best candidates for the construction of our PSF model by visual inspection. The PSF stars are required to be well-isolated stars, to prevent light blending from neighbors, which will degrade the PSF model. They also need to match the ideal shape of a point source at the location of the target.

Finally, the candidates must not be saturated.

Out of the 47 candidates, we found 11 that matched all the criteria and we used them to construct empirical PSF models using the DAOPHOT PSF routine.

As a last quality check, we tested different empirical PSF models with different combinations of the 11 star candidates. We rejected two stars due to their bad residual quality and we tested four different PSF models using different combinations of the nine remaining stars. Finally, we identified the six stars that produce the empirical PSF model with the lowest Chi value. DAOPHOT uses analytical functions to construct a first general approximate PSF model, the Chi value indicates the percentage of the observed stellar profiles that match the analytical function. It is the rms of the residuals that are left after the fitting expressed as a fraction of the peak height of the analytic function. We want to construct an empirical PSF model that better matches the observed stellar profiles of our Keck image, so we want the Chi value to be as low as possible.

The four models gave Chi values of 0.0595, 0.0545, and 0.0491; we chose the stars that gave the smallest value.

All six stars used to construct the empirical PSF model and their residuals after stellar profile fitting subtraction are shown in Figure 2.

3.3. Source-lens Flux Ratio and Separation

As explained in Section 3.1.1, we identified the source star with star 1 in Figure 1 and the lens star with star 2.

We used DAOPHOT's ALLSTAR routine to fit the positions and instrumental magnitudes for all the stars of the frame. A third star in close proximity to the target, which is also identified by the routine, contributes additional flux at the position of the target. We therefore run a 3-star PSF model to ensure simultaneous fit of all three stars. Our 3-star model produced a clean residual, as shown in Figure 1, and the properties of each star are shown in Table 1. The third star is more than 100 mas away from the target, meaning it did not contribute to the lensing event.

Finally, we used DAOPHOT_MCMC (S. K. Terry et al. 2021), a modified version of the DAOPHOT algorithm that contains a Markov Chain Monte Carlo (MCMC) routine, to produce a posterior distribution. We used the validated 3-star PSF model with DAOPHOT_MCMC on each of the 20

Table 1
DAOPHOT Results for the 3-star PSF Fit for the 2020 OSIRIS Images

Component	Coordinates	$F_i/F_{\rm total}$	s_{12} (mas)	s_{13} (mas)	χ^2/ dof
$\rm Star_1$	[1163.52, 1157.06]	0.4247	⋯	⋯	⋯
$\rm Star_2$	[1169.41, 1158.82]	0.1661	⋯	⋯	⋯
$\rm Star_3$	[1156.55, 1169.41]	0.4091	⋯	⋯	⋯
Model	⋯	⋯	54.25	141.23	872.64/855

Note. The pixel coordinates, total flux ratio for each star, the star 1–star 2 and star 1–star 3 separation and χ^2 values for the three-star PSF fitting model. The values are shown for only one image combination of $N-1$ stacked frames.

Table 2
MCMC and Jackknife Results for the 2020 Osiris Images

Parameter	Median	MCMC rms	Jackknife rms	MCMC + JK rms
Separation (mas)	54.200	±0.232	±0.174	±0.290
$\mu_{\rm rel,HE}$ (mas $\rm yr^{-1}$)	7.869	±0.022	±0.052	±0.057
$\mu_{\rm rel,HN}$ (mas $\rm yr^{-1}$)	4.641	±0.014	±0.055	±0.057
$\mu_{\rm rel,helio}$ (mas $\rm yr^{-1}$)	9.144	±0.058	±0.024	±0.063
$\mu_{\rm rel,geo}$ (mas $\rm yr^{-1}$)	9.098	±0.094	±0.059	±0.111
flux ratio	0.388	±0.009	±0.005	±0.011

Table 3
K-band Flux Values

Parameter	Value
K_{S+L}	16.920 ± 0.050
$K_{\rm source}$	17.276 ± 0.050
$K_{\rm lens}$	18.302 ± 0.054

jackknife frames and derived the best-fit values for the source and lens separation and flux ratio. We calculated the MCMC mean and root mean square errors for all 20 frames, and also estimated the uncertainties using the jackknife method (J. Tukey 1958):

$$\sigma_x = \sqrt{\frac{N-1}{N}\sum (x_i - \bar{x})^2}\,, \tag{1}$$

where N is the number of frames, x_i is the parameter value for the ith jackknife stacked image, and $\bar{x}$ is the mean value of the parameter from the jackknife images. Our final uncertainties are the jackknife and MCMC errors added in quadrature as presented in Table 2.

Our estimate for the source and lens separation is 54.203 ± 0.290 mas with a flux ratio of 0.388 ± 0.011. Combining the flux ratio with the blending flux of the target in K band, we found the separate magnitudes of each star to be $K_{\rm star1} = 17.28 \pm 0.050$ and $K_{\rm star2} = 18.30 \pm 0.054$, respectively. In Table 3, we present a summary of the source+lens, source, and lens magnitudes in K band as retrieved from our OSIRIS frames.

3.4. Source and Lens Relative Proper Motion

The source and lens separation measured in the Keck images leads to a heliocentric relative proper motion of $\mu_{\rm rel,helio} = 9.14 \pm 0.06\,\rm mas\,yr^{-1}$, as shown in Table 2. Meanwhile, the light-curve modeling code uses relative proper motions in the geocentric frame, thus we must convert it from heliocentric into geocentric coordinates to compare the measured separation to the light-curve fitting parameters and finally constrain the mass and distance of the lens system.

To do this, we use the relations from S. Dong et al. (2009):

$$\boldsymbol{\mu}_{\rm rel,geo} = \boldsymbol{\mu}_{\rm rel,helio} - \Delta\boldsymbol{\mu} \tag{2}$$

with

$$\Delta\boldsymbol{\mu} = \frac{\pi_{\rm rel}\, V_{\oplus,\perp}}{\rm AU} = \left(\frac{1}{D_{\rm L}} - \frac{1}{D_{\rm S}}\right)\boldsymbol{V}_{\oplus,\perp}, \tag{3}$$

where $\boldsymbol{V}_{\oplus,\perp}$ represents the Earth's orbital velocity projected on the sky at the celestial coordinates of the lens at peak magnification, $D_{\rm S}$ is the distance to the source, and $D_{\rm L}$ is the distance to the lens. We found the velocity expressed in north and east coordinates to be $\boldsymbol{V}_{\oplus,\perp} = (-2.76,\ 8.2)$ km $\rm s^{-1}$ at HJD' = 6905.767. We also used the distance to the lens estimated by A. Bhattacharya et al. (2016). Finally, we use the distance to the source $D_{\rm S} = 8.69 \pm 1.50$ kpc obtained from the Galactic model (N. Koshimoto et al. 2021) that we run using A. Bhattacharya et al.'s (2016) light-curve model results. This gives a geocentric relative proper motion of $\boldsymbol{\mu}_{\rm rel,geo} = |9.098 \pm 0.06|$ mas $\rm yr^{-1}$. This is much higher than the predicted value from A. Bhattacharya et al. (2016), who found $\boldsymbol{\mu}_{\rm rel,geo} = |6.55 \pm 1.12|$ mas $\rm yr^{-1}$. This discrepancy can be explained by the difference between the source crossing times t_* found by our light-curve model ($t_* = 0.027$ days) and by A. Bhattacharya et al. (2016), who found $t_* = 0.04$ days.

4. Light-curve Fitting

In order to determine the precise properties of the OGLE-2014-BLG-1760 planetary system we combine the parameters estimated by the light-curve best-fit model with the AO follow-up measurements. To do this, we follow the method of D. P. Bennett et al. (2024), N. E. Rektsini et al. (2024), and S. K. Terry et al. (2024). We begin by refitting the light curve using the imaged-centered ray-shooting method (D. P. Bennett & S. H. Rhie 1996) and (D. P. Bennett 2010) with the results from A. Bhattacharya et al. (2016) as initial guess. Then, we incorporate the high-angular resolution results to constrain our new light-curve best-fit model. The use of AO constraints help us ensure that all the accepted light-curve models will be in agreement with the lens properties determined by the high-angular resolution study.

Table 4
Light-curve Best-fit Model Parameters

Parameter	MCMC (lc)	MCMC (lc + AO)	Bhattacharya+16
t_E (days)	13.50 ± 0.40	13.47 ± 0.08	15.87 ± 0.41
t_0(HJD')	6905.767 ± 0.029	6905.770 ± 0.027	6905.856 ± 0.026
u_0	0.2199 ± 0.0106	0.2203 ± 0.0014	0.1806 ± 0.0074
s	0.7946 ± 0.0061	0.7944 ± 0.0012	0.8269 ± 0.0047
θ (rad)	-0.4029 ± 0.0106	-0.4052 ± 0.0071	-0.3977 ± 0.0086
$q \times 10^{-4}$	11.61 ± 1.27	11.06 ± 1.09	8.64 ± 0.89
t_* (days)	0.0274 ± 0.0023	0.0273 ± 0.0017	0.0366 ± 0.0044
I_s	18.85 ± 0.06	18.79 ± 0.05	19.07 ± 0.14
V_s	20.09 ± 0.06	20.19 ± 0.06	20.51 ± 0.26
$\pi_{E,E}$	⋯	0.0450 ± 0.0058	⋯
$\pi_{E,N}$	⋯	0.0251 ± 0.0033	⋯
π_E	⋯	0.052 ± 0.005	5.86
D_S(kpc)	⋯	7.943 ± 1.708	⋯
χ^2	26179/26344	26180/26341	⋯

Note. We show the MCMC mean values and 1σ results for the best-fit obtained using only the light-curve data (Column (1)), the light-curve data and the constraints derived by our 2020 Keck follow-up images (Column (2)), and the results presented by A. Bhattacharya et al. (2016) in the discovery paper (Column (3)).

We use a modified version of the light-curve modeling code (D. P. Bennett & S. H. Rhie 1996; D. P. Bennett 2010), named `eesunhong`,[12] in honor of the original coauthor of the code (D. P. Bennett 2014; D. P. Bennett & D. Khavinson 2014). The code combines the microlensing event data sets with the relative proper motion and lens flux obtained by the AO follow-up analysis and uses them to constrain both the light-curve parameters and the lens properties. Due to the tight relation between the relative proper motion and the microlensing parallax, the code is capable of finding the microlensing parallax even in cases when it is not observed in the light curve. In order to fit the microlensing parallax, we need to also include the distance to the source D_S as a fit parameter. This is because the parallax vector is parallel to the relative proper motion in the inertial geocentric frame $\boldsymbol{\mu}_{\rm rel,geo}$, while the Keck images measure $\boldsymbol{\mu}_{\rm rel,helio}$ in the heliocentric frame. The conversion between $\boldsymbol{\mu}_{\rm rel,geo}$ and $\boldsymbol{\mu}_{\rm rel,helio}$ requires D_S. Finally, the code uses an MCMC algorithm with a Metropolis Hastings sampler to inspect the posterior distributions of both the light-curve fitting parameters and the physical parameters of the planetary system. A detailed description of this code and the required parameters is included in D. P. Bennett et al. (2024).

Here, we illustrate the parameters of the light-curve fit and present the results from models both with and without the use of the AO follow-up constraints, in addition to an extended study of the angular source radius.

4.1. Light-curve Model Parameters

There are three parameters that apply to both a single lens and an N-lens microlensing event. These are t_E, the Einstein crossing time (length of the event), t_0, the moment of the minimum separation between source and lens, and u_0, the impact parameter that defines the minimum source-lens separation in units of the angular Einstein ring radius. In cases where the source star crosses a caustic or a cusp of a multiple lens, finite source effects may be observed in the light curve, giving t_*, the crossing time of the source radius. We can also estimate the angular source size θ_* using the T. S. Boyajian et al. (2014) surface brightness relations for main-sequence stars:

$$\log(2\theta_*) = 0.5014 + 0.419(V - I)_S, 0 - 0.2I_{S,0}, \quad (4)$$

where $(V - I)_{S,0}$ is the dereddened color of the source and $I_{S,0}$ the dereddened source magnitude in I band. There are three additional parameters that define a binary lens system: the planet–host star mass ratio q, their projected separation s calculated in angular Einstein radius units, and finally the angle α between their separation vector and the source trajectory. Finally, we fit two additional observational parameters, the flux of the source F_s and the blending flux F_b. The blending flux can contain the lens flux in addition to other star fluxes located in close proximity to the target. The final time-varying magnification that defined the microlensing event is expressed as $F(t) = A(t)F_s + F_b$.

4.2. Light-curve Best-fit Model

We begin by fitting the light-curve data without the constraints from the high-angular resolution images, using the results from A. Bhattacharya et al. (2016) as an initial guess for the two lens–one source (2L1S) fit. We use the same data sets as in A. Bhattacharya et al. (2016; discussed in Section 2), but we use a re-reduction of the MOA data set as described in I. Bond et al. (2017). Our MOA photometry has improved systematics after detrending to remove correlations with seeing and hour angle. The use of the re-reduced MOA data set had an important impact in our new light-curve model, as shown in Column (1) of Table 4. We already observe differences between our best-fit model and the results presented in the discovery paper. We attribute these differences to the improved MOA photometry. We present the posterior distributions of our new light-curve model in Figure 3 and the 2L1S light-curve fit in Figure 4.

We proceeded to refit the light curve including the high-angular resolution follow-up results, using the modified version of the `eesunhong` code. The use of the relative proper motion and lens flux measurements provide stronger constraints on the best-fit models and ensures consistent estimates of the lens and source properties. It also allows us to fit the microlensing parallax, even if this is not observed during the microlensing event, when including the distance to the

[12] https://github.com/golmschenk/eesunhong

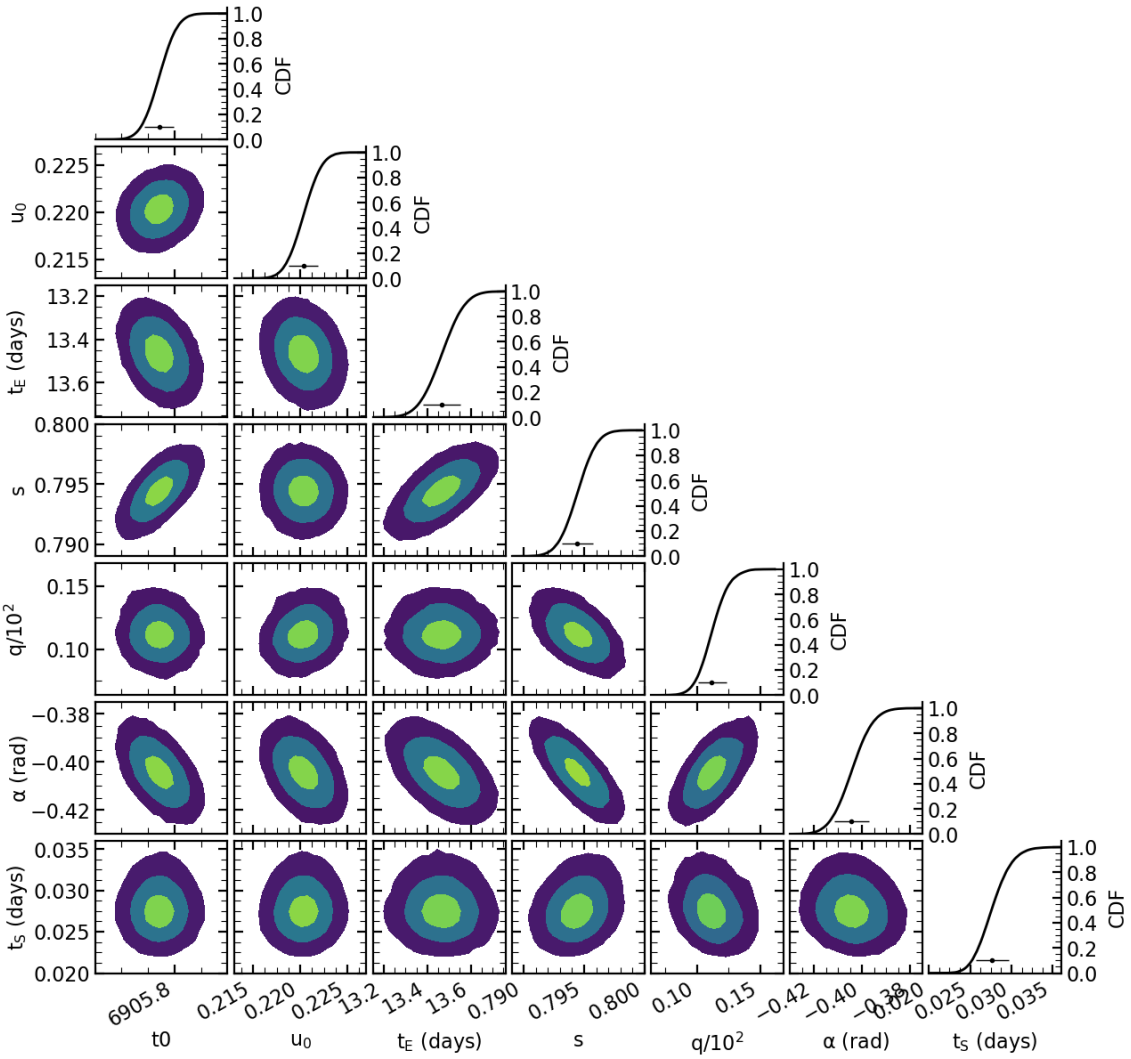

Figure 3. The marginalized posterior distributions of the new light-curve best-fit model. On the diagonal we show the one-dimensional cumulative density function of each parameter. The 68.3% (1σ), 95.5% (2σ), and 99.7% (3σ) confidence intervals are represented by dark violet, median blue, and light green, respectively.

source D_S as a fit parameter. Since neither the distance to the source nor the microlensing parallax are directly observed for this event, we use the priors obtained from N. Koshimoto et al.'s (2021) Galactic model, using `genulens`[13] (N. Koshimoto & C. Ranc 2022). We use I_S and $(V - I)_S$ values from (A. Bhattacharya et al. 2016) in the Galactic model and obtain $D_S = (8.69 \pm 1.56)$ kpc for the distance to the source and $(\pi_{E,E}, \pi_{E,N}) = [(3.579, 2.591) \pm (7.321, 6.774)] \times 10^{-2}$, respectively, for the east and north parallax components. A probability distribution of the priors of the parallax components is shown in Figure 5. The best-fit light-curve model parameters with the AO constraints are presented in Column (2) of Table 4. We can see that the two sets of parameters produced for the light-curve models, with and without AO constraints, are in perfect agreement.

We find the Einstein crossing time t_E to be 2.40 days shorter than the one reported by A. Bhattacharya et al. (2016), which has a significant impact on the mass ratio q, which is 28% larger than the previous value. We find a separation s of 0.7943 angular Einstein radius, which confirms that $s < 1$. We also find a 22% larger impact parameter u_0, which is largely based on the MOA re-reduction, since the MOA R band dominates the peak of the light curve. We also report significant changes in the finite source effects, where we find the source crossing time t_* to be 0.93×10^{-2} days smaller than the one reported in A. Bhattacharya et al. (2016). We find a microlensing parallax of $\pi_E = 0.052 \pm 0.005$ which is close to the value estimated by the Galactic model ($\pi_E = 0.111 \pm 0.087$), also shown in Figure 5, and we confirm that A. Bhattacharya et al. (2016) correctly rejected the large, doubtful parallax value of $\pi_E = 5.86$ that was inferred from the original light curve.

Finally, we use the same calibration relations as in A. Bhattacharya et al. (2016) to convert OGLE-IV magnitudes to OGLE-III catalog Cousins I and Johnson V magnitudes. We observe small differences in the source I and V brightness, where we find a 0.32 less bright source in V band and 0.28 difference in I band. This implies a source color $(V - I)_S = 1.40 \pm 0.06$.

4.3. Source Angular Size

Regarding the source angular radius θ_*, we compare the values estimated via our AO follow-up constraints and the

[13] doi:10.5281/zenodo.6869520

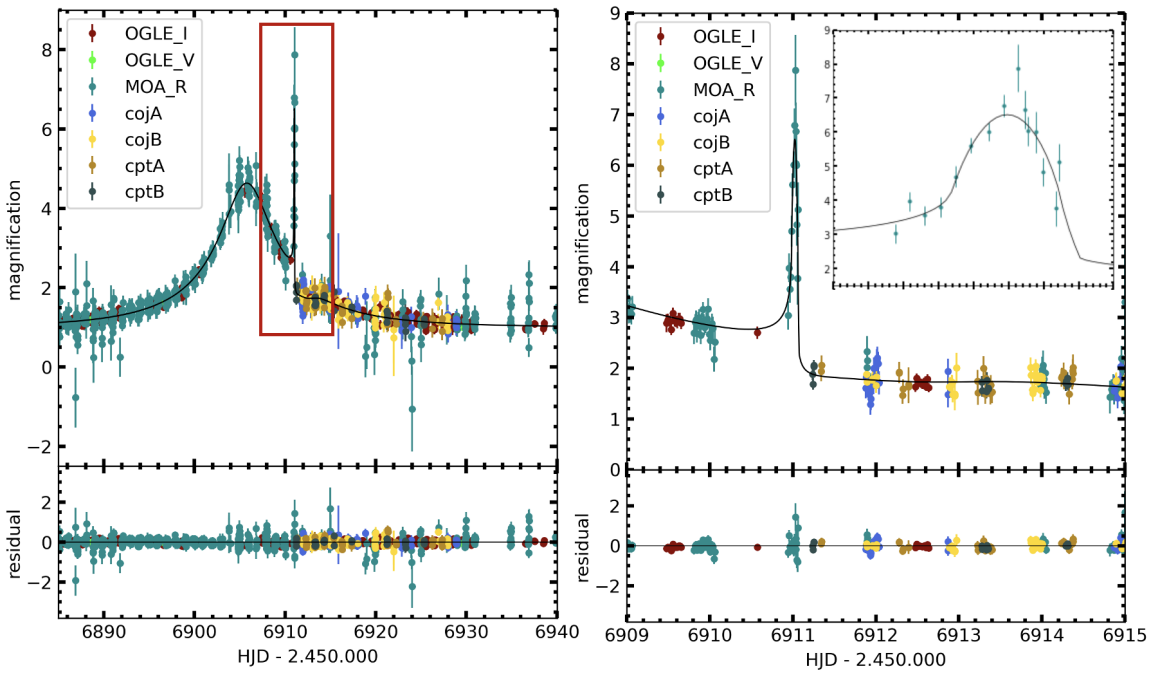

Figure 4. Best-fit model of the light curve of OGLE-2014-BLG-1760. The 2L1S best-fit model is indicated by the black curve. The bottom panel shows the residual from the best-fit model and the OGLE, MOA, and RoboNet data. The right panel presents the enlargement of the caustic-crossing and the cusp of the light curve and the top right-corner panel shows a close-up of the anomaly. The figures were produced using the software described in C. Ranc (2020).

source color and brightness. We combine the Einstein crossing time and source crossing time from the new light-curve model with the constrained angular Einstein ring radius from the AO follow-up results and we can calculate θ_* using the relation :

$$\theta_* = \theta_{\rm E} \times \frac{t_*}{t_{\rm E}}, \tag{5}$$

where $\theta_{\rm E} = 0.336 \pm 0.002$ mas, as shown in Table 5. We find $\theta_* = 0.673 \pm 0.004$ microarcseconds (μas), which is very close to the value of 0.657 ± 0.011 μas predicted by A. Bhattacharya et al. (2016). In addition, we also estimate the source angular radius θ_* using Equation (4) for $I_{\rm S,0} = 17.34 \pm 0.02$ and $(V-I)_{\rm S,0} = 0.26 \pm 0.06$, finding $\theta_* = 0.693 \pm 0.004$ μas.

The small difference of 0.02 μas between the two θ_* values, which is less than 2σ, confirms that the source color must be quite blue and hints toward the probability that the source star is located in the far Galactic disk, beyond the Galactic bulge and outside the bulge.

5. Lens System Properties

5.1. Lens Mass–Distance Relations

Planets discovered via the microlensing technique are usually located at 1–7.5 kpc distance. For this reason, we characterize the microlensing planetary systems by measuring the mass and distance of the lens, in addition to the planet's orbital distance to the host star. As we mentioned briefly in the introduction, it is possible to use empirical mass–distance relations for the lens to better constrain the physical parameters of the system.

The first method to estimate the lens properties comes from the source-lens relative proper motion. A precise measurement of the geocentric relative proper motion leads to the angular Einstein radius $\theta_{\rm E}$, since $\theta_{\rm E} = \mu_{\rm rel,geo} \times t_{\rm E}$, from which we can derive the mass and distance relation:

$$M_{\rm L} = \frac{\theta_{\rm E}^2}{\kappa \pi_{\rm rel}}, \tag{6}$$

where $\pi_{\rm rel} = {\rm AU}\,({D_{\rm L}}^{-1} - {D_{\rm S}}^{-1})$ for source and lens distances in kpc, and $\kappa = \frac{4G}{c^2 AU} = 8.144$ mas $M_\odot^{-1}$.

The second relation depends on the microlensing parallax. This can be observed for long timescale events where the parallax will occur naturally due to the Earth's orbit as in N. Koshimoto et al. (2017b). It can also be observed by simultaneous ground-based and space-based observations of microlensing events (A. Udalski et al. 2015; R. A. Street et al. 2016). The measurement of the microlensing parallax can provide a strong relation between the distance and the mass of the lens due to its definition:

$$\pi_{\rm E} = \sqrt{\frac{\pi_{\rm rel}}{\kappa M_{\rm L}}}. \tag{7}$$

There are very few events with precise microlensing parallax detection from the ground, so for short duration events like OGLE-2014-BLG-1760 that do not have observations from space during the lens event, the parallax mass–distance relation requires additional information such as that provided by high-angular resolution flux constraints.

Finally, the measurement of the lens magnitude $m_{\rm L}(\lambda)$ can be used in a mass–luminosity function for different ages and metalicities of main-sequence stars (X. Delfosse et al. 2000). Furthermore, we can combine the mass–luminosity relation with stellar isochrones (L. Girardi et al. 2002) of main-sequence stars and construct a third mass–distance relation:

$$m_{\rm L}(\lambda) = 10 + 5\log_{10}(D_L/1\ {\rm kpc}) + A_{\rm KL}(\lambda) + M_{\rm isochrone}(\lambda, M_{\rm L}, age, [{\rm Fe/H}]), \tag{8}$$

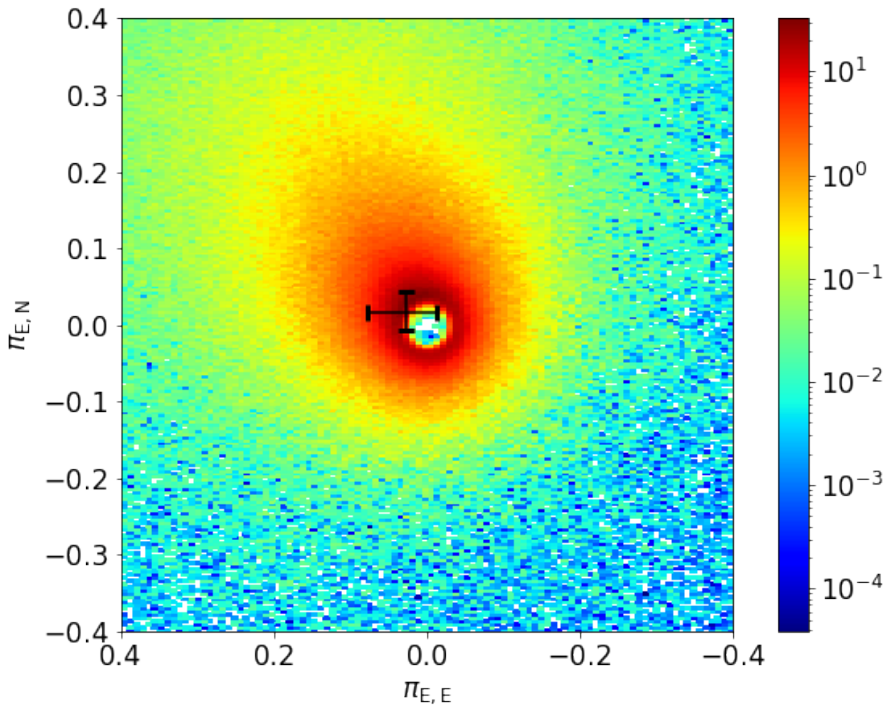

Figure 5. Two-dimensional parallax distribution based on the Galactic model (`genulens`). The color-scale shows the relative probability, the black cross indicates the microlensing parallax coordinates predicted using our (AO) Keck constraints.

Table 5
Lens Parameters

Parameters	Units	Values and 1σ
Angular Einstein radius $\theta_{\rm E}$	mas	0.336 ± 0.002
Host mass M_h	$M_\odot$	0.803 ± 0.097
Planet mass m_p	$M_{\rm Jup}$	0.931 ± 0.117
Lens distance $D_{\rm L}$	kpc	7.056 ± 1.468
Two-dimensional separation $\alpha_\perp$	au	1.887 ± 0.380

where $A_{K_{\rm L}}(\lambda)$ is the K-band lens extinction and $M_{\rm isochrone}$ is the absolute magnitude in λ wavelength.

The extinction to the lens $A_{K_{\rm L}}(\lambda)$ is estimated by combining the extinction in K band with the distance to the source and the distribution of the Galactic dust in relation to the source and lens locations. If we assume the Galactic dust distribution as an exponential in both radius and height in a disk (R. Drimmel & D. N. Spergel 2001), then the extinction to the lens can be approximated as:

$$A_{K_{\rm L}} = \frac{1 - e^{-|D_{\rm L}(\sin b)/h_{\rm dust}|}}{1 - e^{-|D_{\rm S}(\sin b)/h_{\rm dust}|}} A_K, \tag{9}$$

where $b = -2\overset{\circ}{.}2746$ is the Galactic latitude of the event, $h_{\rm dust} = 0.10 \pm 0.02$ kpc is the dust scale height, $D_{\rm S}$ is the distance to the source from the light-curve model, and A_K is the K-band extinction at the distance to the source. In Figure 6, we show the mass and distance graph of the lens system by combining the three mass and distance relations described here. We present the microlens parallax constraint in aquamarine and the angular Einstein radius constraint in gold. Finally, we present the isochrone constrained mass–luminosity relation with purple line and red dotted lines to express the errors in the magnitude of the lens. We calculate the mass–luminosity relation for a lens extinction in K band equal to $A_{K_{\rm L}} = 0.165$ using the Equation (9) and we use isochrones for ages up to 10 Gyr and metallicities within the range $0.0 \leqslant [{\rm Fe/H}] \leqslant +0.3$. This is consistent with the estimates of W. I. Clarkson et al. (2011), where the authors find very few stars with ages less than 5 Gyr inside the Galactic bulge but the varying metallicities observed by microlensed stars show that there should be a significant number of intermediate age (5–8 Gyr) stars hidden inside the bulge (T. Bensby et al. 2013).

5.2. Planetary System Parameters

By combining the light-curve fitting parameters with the high-angular resolution observations using the mass–distance relations, we find that the lens system is characterized by a Jupiter–Sun analog with a planet of mass $M_p = 0.931 \pm 0.117\ M_{\rm Jup}$ orbiting a host star of mass $M_* = 0.803 \pm 0.097\ M_\odot$, as shown in Table 5. We find the system residing inside the Galactic bulge at distance $D_{\rm L} = 7.056 \pm 1.468$ kpc, making it one of the most distant planetary systems discovered to date. Finally, we calculate the projected separation between the planet and the host star as:

$$\alpha_\perp = s D_{\rm L} \theta_E. \tag{10}$$

We find the Jupiter-mass planet to be in an orbital distance of $\alpha_\perp = 1.887 \pm 0.380$ au around its host star.

The probability distributions, in red, for the mass and distance of the lens and the planet and host star orbital separation presented in Figure 7 are the product of the three empirical mass–distance relations combined with the constrained light-curve fitting parameters. Our results show a difference between the expected values from A. Bhattacharya et al. (2016). This can be partly explained by the differences in the light-curve model estimates and in particular the length of the event, which affects the planet–host star mass ratio and the source radius crossing time.

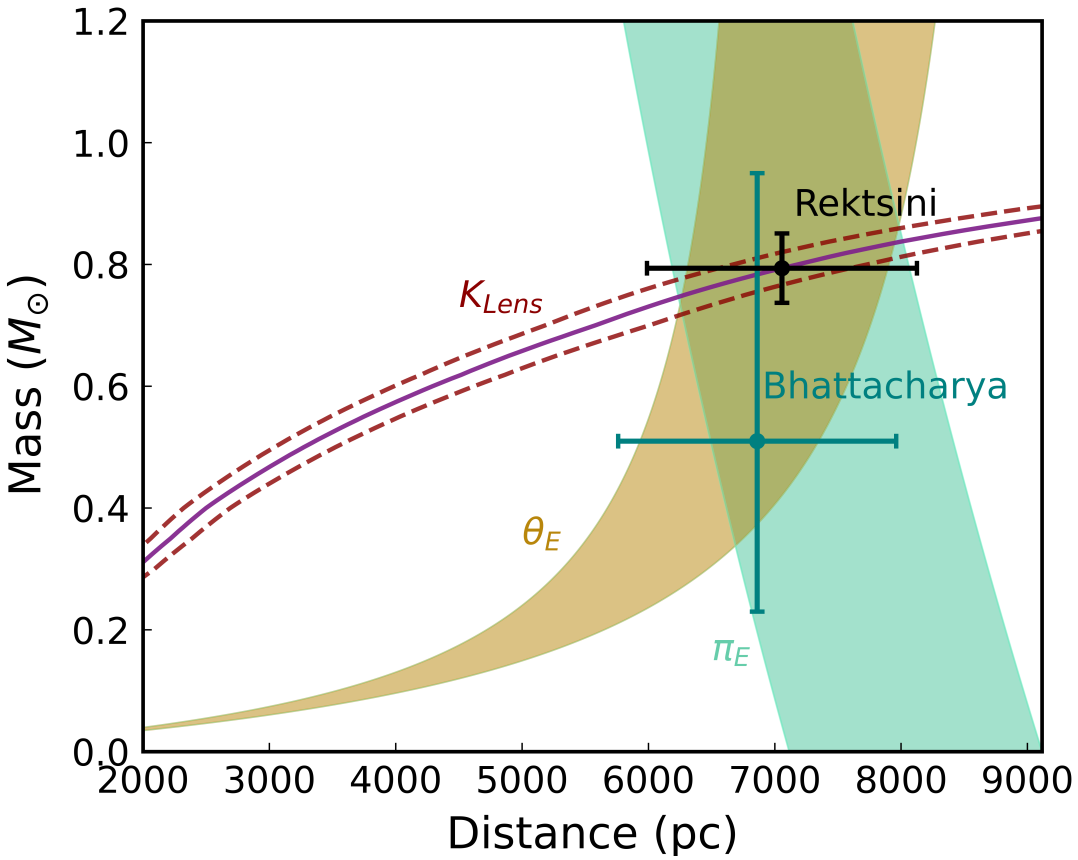

Figure 6. Mass–distance estimate for the lens. The purple curve represents the constraint from the *K*-band lens flux measurement for isochrones up to 10 Gyr, the red dotted lines represent the flux uncertainties, the gold curve shows the Einstein angular radius measurement, and the aquamarine curve represents the microlensing parallax constrained by the (AO) results. The intersection between the three curves defines the estimated solution of the lens physical parameters.

Meanwhile, in this figure, we also notice that while the Keck follow-up results manage to derive the mass of the lens very accurately, the distance to the lens seems to be better constrained by the Bayesian Galactic model, plotted in gold. We remind that this is a very faint and highly blended event with a poorly constrained source color, which leads to significant questions about the properties of the source star. The Galactic model relies only on the light-curve information (I_s,$(V-I)_{S,0}$,t_E, θ_E and the event's galactic coordinates), and thus derives statistically the most probable scenario for this set of parameters. In our case this would be a less massive lens, located almost inside the Galactic bulge and a source star located in the far disk. This low lens mass scenario is rejected by the AO follow-up results, which revealed a much more massive lens. This implies that the lens and source stars should be closer to each other (Equation (6)), which, as a result, increases the uncertainty in both source and lens distance measurements. The constraints that we obtain from the Keck follow-up analysis are not affected by the size of the magnification or the quality of the light-curve data, which is also the main interest of these observations, but an accurate lens distance measurement requires an accurate source distance, due to their tight relation. This means that we need to study further the source star properties in order to accurately constrain the planetary system parameters.

6. Source Star Properties

As explained in A. Bhattacharya et al. (2016) and shown in Figure 8, there are no MOA-V observations for this event and the few OGLE-V points contain large uncertainties. In addition, the event is very faint and the source highly blended. This produces a lot of uncertainties in the source color and brightness. We decided to study further the source color and distance using AO follow-up constraints with the light-curve model, the Bayesian analysis with N. Koshimoto et al.'s (2021) Galactic models and the Gaussian mixture approach.

6.1. Source Color

Here, we use the catalog from F. Surot et al. (2020) to find the extinction to the source in K band. For the galactic coordinates of the event $l = 1.^{\circ}3186$, $b = -2.^{\circ}2746$, we find $E(J-K) = 0.3350 \pm 0.0100$ for a distance $r = 0.00072$ between the F. Surot et al. (2020) grid point and the target in degrees. From S. Nishiyama et al. (2009), we find the $A_K/E(J-K) = 0.494$ relation and finally the K-band extinction as $A_K = 0.165$. This means that according to A. Bhattacharya et al.'s (2016) results we expect the source magnitude in K band to be $K_S = 17.425 \pm 0.08$.

We also estimate the K band of the source using the source color predicted by our new light-curve model as described in Section 4. For $(V-I)_{S,0} = 0.26 \pm 0.06$, we find $(V-K)_{S,0} = 0.465$ using the color tables from M. J. Pecaut & E. E. Mamajek (2013). This leads us to a flux value for the source of $K_S = 17.24 \pm 0.06$, which is much closer to the K-band magnitude measured in the Keck high-angular resolution images. Finally, we use the angular source radius implied by the AO constraints in Section 4.2 and the $I_{S,0}$ value from the light-curve model as known parameters in

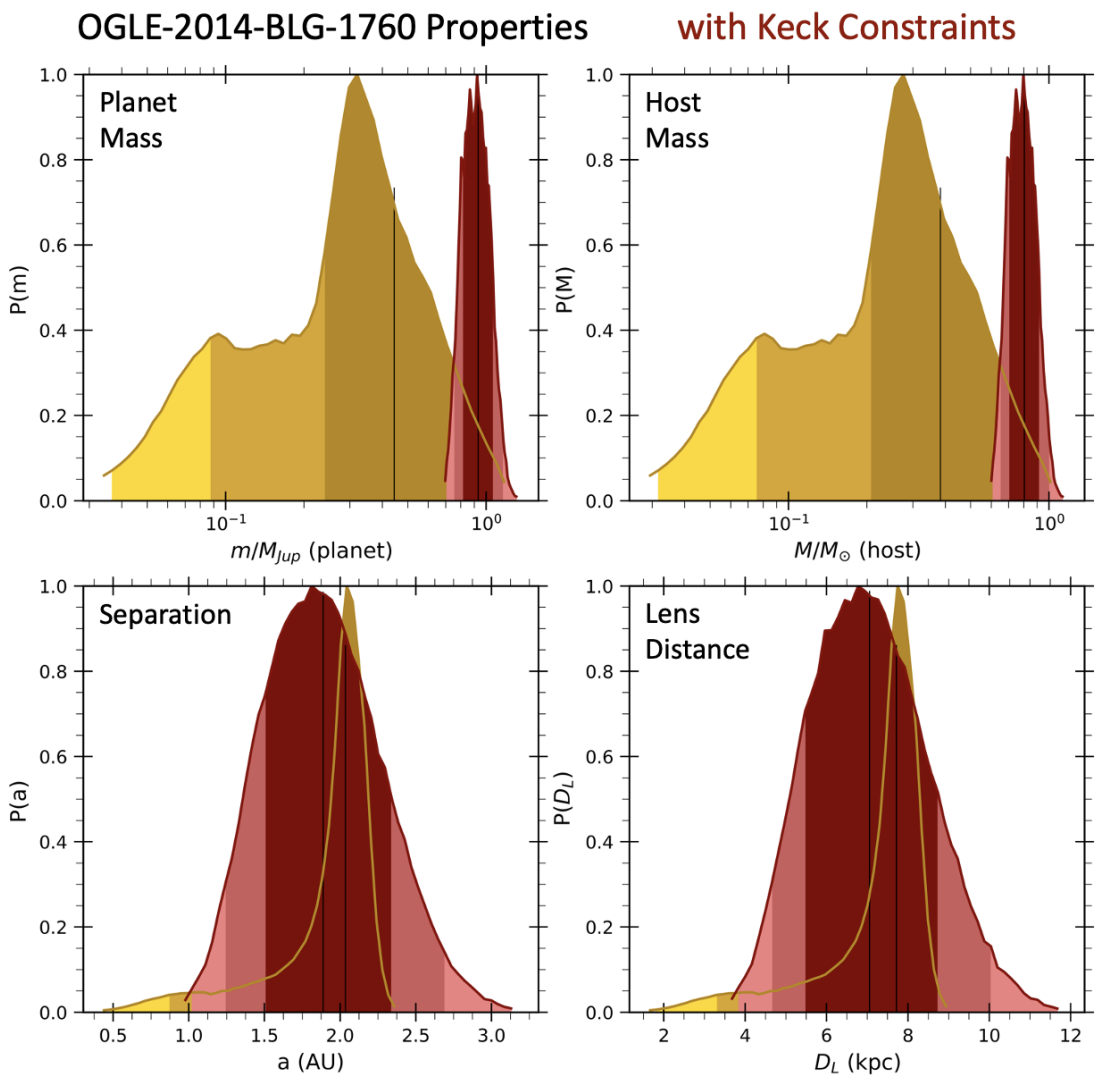

Figure 7. Bayesian posterior probability distributions for the planetary companion mass, host mass, their projected separation, and the distance to the lens system are shown with only light-curve constraints in gold and with the additional constraints from our Keck follow-up observations in red. The centers 68.3% (1σ) of the distributions are shaded in darker colors (dark red and dark gold), and the remaining central 95.4 % (3σ) of the distributions are shaded in lighter colors. The vertical black line marks the median of the probability distribution for the respective parameters. The priors used for the Bayesian analysis are the estimates from the final light-curve model. We show that the medians of the Bayesian probability are within 2σ of the constrained parameter distributions for the lens mass and distance.

Equation (4) and we derive a new estimate for the source color of $(V-I)_{S,0} = 0.228 \pm 0.070$. This new color estimate aligns with the source having a very blue color.

We derive that the K-band magnitude of the source for this color should be $K_S = 17.30 \pm 0.06$. A summary of the results for the angular source radius θ_*, the source color $(V-I)_{S,0}$, and source K_S magnitudes calculated for each case can be found in Table 6. Our K_S source magnitude estimates from both cases are consistent with the magnitude deduced in Section 3.3 using the OSIRIS images, and thus tend to confirm the blue color of the source star. Using the color tables from https://www.pas.rochester.edu/~emamajek/EEM_dwarf_UBVIJHK_colors_Teff.txt based on M. J. Pecaut & E. E. Mamajek (2013), we estimate the source star to be an A7-dwarf with effective temperature of $T_{\rm eff} \sim 7760$ K and radius of $\sim 1.750 R_\odot$.

6.2. Source Distance from the Galactic Models

We investigate further the galactic location of the source by running a new Galactic model using `genulens` (N. Koshimoto et al. 2021; N. Koshimoto & C. Ranc 2022). We study the source distance for all three source colors and magnitudes presented above. As shown in Table 6, the Bayesian analysis using the Galactic model predicts a source star located inside the Galactic bulge according to the source color adopted by A. Bhattacharya et al. (2016) but the distance increases for the new source color, both from the new light-curve model and the AO follow-up results. More precisely, we find that for a $(V-I)_{S,0} = 0.228 \pm 0.06$ and $I_{S,0} = 18.74 \pm 0.06$, the distance to the source is $D_S = 10.321^{+1.983}_{-0.721}$ kpc, while the distance increases to 11 kpc for the source color inferred from our new light-curve model, without including the AO follow-up constraints. Since the Galactic models do not predict a source location on the far side of the bulge (A. Bhattacharya et al. 2016), we explored the source color parameter space in order to estimate the break point, where the model "jumps" to distances larger than 8 kpc. We fixed $I_{S,0} = 18.74 \pm 0.06$ and explore the effect of increasing the color by increasing $V_{S,0}$. We find that the model predicts a source closer than 9 kpc for $V_{S,0} = 17.82$, which gives a source color $(V-I)_{S,0} = 0.48 \pm 0.10$. This leads

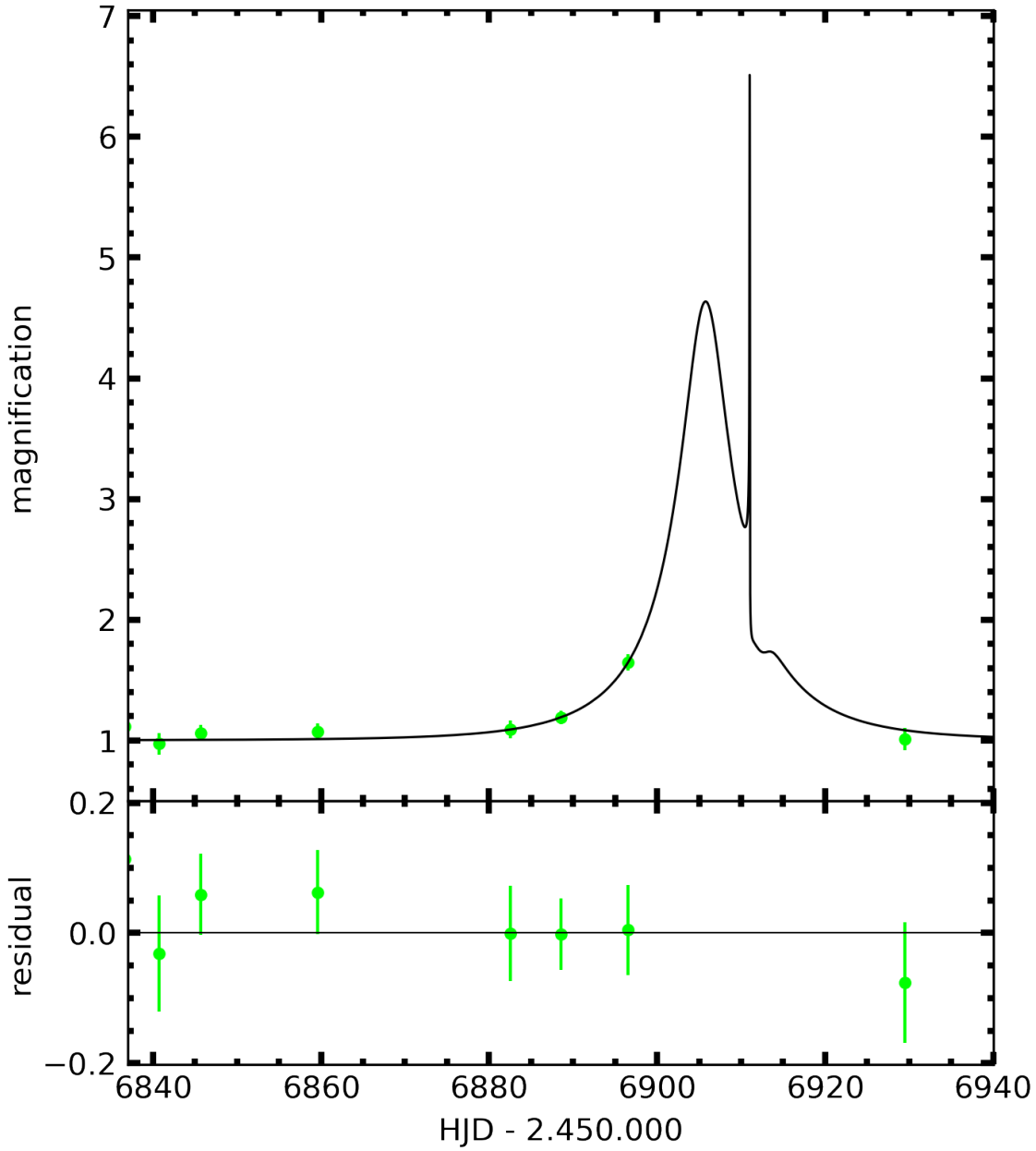

Figure 8. 2L1S light-curve model described by the black line with the *V*-band data. The green points showing the OGLE-V data around the microlensing event, the only *V*-band observations. In the bottom panel, we show the residual from the best-fit model and the OGLE-V data.

Table 6
Source Properties

Parameter	$\theta_*(\times 10^{-4}$ mas)	$(V-I)_{S,0}$	K_S	D_S (genulens) (kpc)	D_S (pyLIMASS) (kpc)
A. Bhattacharya et al. (2016)	6.57 ± 0.11	0.34	17.425 ± 0.08	$8.69\ ^{+1.449}_{-0.761}$	9.59 ± 2.39
Light curve	6.932 ± 0.040	0.26 ± 0.06	17.24 ± 0.06	$11.53\ ^{+1.725}_{-1.244}$	11.94 ± 1.72
AO follow-up	6.728 ± 0.040	0.228 ± 0.070	17.30 ± 0.06	$10.32\ ^{+1.983}_{-0.721}$	10.67 ± 2.32

Note. The angular size, color, magnitude in *K* band and distance of the source predicted by the A. Bhattacharya et al. (2016) analysis, by our updated light-curve model, and by the AO follow-up constraints. The source color value from the last method gives the closer *K*-band source magnitude to $K_S = 17.28$ measured in the Keck images.

to a predicted infrared magnitude $K_S = 18.99$ value, according to M. J. Pecaut & E. E. Mamajek's (2013) color tables, which is ruled out by our Keck AO imaging. In all cases, the lens distance remains around 7 kpc, demonstrating that the inferred planetary system parameters are robust to systematics in the source color.

6.3. Source Distance from the Gaussian Mixture Approach

Here, we study the source and lens properties using a different approach by using the pyLIMASS algorithm.[14] This tool is independent from Galactic models and uses isochrones to model the stellar properties while using a list of observables as constraints. Finally, it uses a Gaussian mixture approach to approximate the posterior distribution, sampling the most plausible physical parameters of the lens and source. Furthermore, it uses a different statistical approach to combine the source and lens fluxes from the light-curve model and the AO follow-up images with the isochrones to produce the final stellar property distributions. A detailed description of the code can be found in E. Bachelet et al. (2024). The estimates here are mostly based on the isochrones.

We run pyLIMASS using as observables the I_S magnitude, the $(V-I)_S$ source color, the t_E Einstein time and $\rho = t_*/t_E$ values, all parameters fitted by the light-curve model, in addition to the source and lens K-band magnitudes measured from the AO follow-up images. Our results for the source and lens distance are compatible with the Galactic model analysis. pyLIMASS finds the source located further away from the Galactic bulge in all three cases, but finds a slightly smaller distance for the color from A. Bhattacharya et al. (2016). Furthermore, the code estimates a lens mass of $0.9 \pm 0.2\ M_\odot$, which is in agreement with our AO+lc analysis and a source surface temperature of $T_{\rm eff} = 7900 \pm 500$ K, in agreement with the results in Section 6.1.

The weight of the evidence, even though it fails to constrain the source distance value, strongly suggests that OGLE-2014-BLG-1760 is the first microlensing event with AO follow-up observations that confirm an early-type source star located behind the Galactic bulge.

7. Summary and Conclusion

Our Keck AO follow-up observations of OGLE-2014-BLG-1760 5.94 yr after the microlensing peak have allowed us to separately identify the source and lens and reveal their characteristics. Our K-band observations with Keck OSIRIS imager show a lens of magnitude $K_{\rm lens} = 18.30 \pm 0.05$ and a source magnitude of $K_{\rm source} = 17.28 \pm 0.05$. The separation between source and lens was larger than predicted in the discovery paper (A. Bhattacharya et al. 2016), leading to a 2.5 times larger relative proper motion of $\mu_{\rm rel} = \mid 9.14 \pm 0.05 \mid$ mas yr^{-1}. This discrepancy can be resolved by the significant differences in the source size and the length of the event in our new light-curve model.

We used a modified version of the imaged-centered ray-shooting method (D. P. Bennett & S. H. Rhie 1996; D. P. Bennett 2010) that uses the source and lens magnitudes and their relative proper motion as additional constrains to fit the light-curve model. Furthermore, the use of the re-reduced R-MOA data set has had a significant impact in our fitted light-curve parameters reducing the length of the event by $\sim$2.4 days. This is probably due to the short Einstein time and the faintness of the event and also the fact that the R-MOA data are dominating the light magnification. This means that even small detrending corrections can sometimes result in important alterations in the parameters that define the event. We find a larger planet–host star mass-ratio value of $q = (11.06 \pm 1.09) \times 10^{-4}$, which places the event even further away from the mass-ratio break point found in D. Suzuki et al.'s (2016) sample, making the event a Sun–Jupiter analog.

The use of AO follow-up constraints for our light-curve fit has permitted us to derive the microlens parallax of the event, which in return worked as an additional constrain for the lens mass and distance. Our light-curve model yields a parallax value of $\pi_E = 0.052 \pm 0.005$, a value that is also confirmed by our Galactic model. Using this parallax value in addition to the lens K-band magnitude and relative proper motion, we find the lens to be described by a Jupiter-mass planet of $M_p = 0.931 \pm 0.117\ M_{\rm Jup}$ orbiting an early K-dwarf star of $M_* = 0.803 \pm 0.097\ M_\odot$ in $D_L = 7.056 \pm 1.468$ kpc. This places the lens in the Galactic bulge or in the bar. The confirmation of a microlensing planet in the Galactic bulge region contradicts the claims of M. T. Penny et al. (2016)—there are planets in the inner Galactic bulge region. Finally, the rather large uncertainty in our lens distance estimate is probably caused by the highly uncertain source position. This shows the importance of the precise characterization of the source properties in order to constrain the lens system physical parameters.

It is not easy to derive the source properties of this microlensing event. OGLE has obtained few measurements in V band and all the points are at low amplification, which hampered the possibility to obtain a secure V-band source estimate from the light-curve fit (Figure 8). Our new light-curve model also derived a quite blue source color of $(V-I)_S = 1.4 \pm 0.06$ but this value is also dependent from the same V data used in the discovery paper. In our attempt to validate this result, we decided to estimate the source color independently from the OGLE V-band observations.

We use the source magnitude measured from Keck images as a reference. We derive the K band of the source using the source color from the light-curve model, the value is inside the 2σ difference from the Keck K-band value. Then, we also use the source angular radius value θ_* that we derive using the relative proper motion of the AO follow-up images, and we use this value and Equation (4) with the I_S of the light curve to calculate a new estimate for the source color. Finally, we use this source color to deduce the K magnitude of the source. As shown in Table 6, both methods reveal K-band values for the source that are inside 2σ from the initial Keck images value.

If we estimate the source color to be $(V-I_C)_{S,0} \sim 0.24$, thgen according to M. J. Pecaut & E. E. Mamajek (2013) we expect the source star to be an A7-dwarf of $\sim 1.75 R_\odot$ radius. This result reinforces the case of the source being a young star residing in the Galactic disk, behind the Galactic bulge. Meanwhile, this scenario is also favored by our Galactic model (N. Koshimoto et al. 2021). We used the derived I_S and source color values for all three cases presented above and find the most probable estimate of the source distance to be in $D_S = 10.321^{+1.983}_{-0.721}$ kpc. Finally, we also compared the source distance with the predictions derived by pyLIMASS. The advantages of comparing the source and lens properties with this tool are that it is independent of the Galactic models, giving more emphasis on stellar isochrone models, and it uses a different statistical method from both eesunhong (MCMC algorithm with a Metropolis Hastings sampler) and genunlens (Bayesian analysis) to produce the stellar properties distributions. Finally, pyLIMASS combines information from

[14] https://github.com/ebachelet/pyLIMA

both the light-curve model and the constrained *K*-band source value from the Keck images. This means that, contrary to the Bayesian analysis with a Galactic model, it is able to reject the false smaller lens mass scenario and make more accurate predictions for the nature of the source star. Our results with `pyLIMASS` are in agreement with the lens properties inferred from the light-curve model and the AO follow-up analysis, while they also favor the source star being located behind the Galactic bulge. Finally, we examine the stellar color and *I*-band properties of the stars residing inside the Galactic bulge (Figure 7, left panel from S. K. Terry et al. 2020) and we find no star exhibiting similar properties in that field.

There have been studies (M. G. Navarro et al. 2020) as well as a few previous reports of microlensing events that could contain source stars in the far disk. Y. Shvartzvald et al. (2018) were the first to report the discovery of a giant planetary system, probably inside the Galactic bulge, and a source suffering from a severe reddening that placed it in the far disk, behind the bulge. As mentioned in their paper, the field around this event suffers from high and differential extinction, which makes it very challenging to derive precise properties for the source star, but their results seem to indicate an M7 giant dwarf located in the far disk. Similarly, D. P. Bennett et al. (2018) report the discovery of a microlensing event with an unusually red source color, which makes it impossible for the source star to be inside the Galactic bulge. They mention that one possible option would be for the source to reside in the far disk but they also favor the scenario of a lower main-sequence source star in front of the Galactic bulge. Finally, S. S. Li et al. (2019) report the discovery of a microlensing event with a variable oscillating red giant source star that could potentially be located behind the Galactic bulge.

OGLE-2014-BLG-1760 is the only event, so far, with AO follow-up observations that suggest a source star located in the far disk. Furthermore, the color and the *K*-band magnitude of the source indicate a young early A-dwarf star, which are very common in this Galactic region. Further observations with high-angular resolution images in multiple bands will be able to confirm these results and offer a final precise measurement for the source and the lens distance.

As mentioned in A. Bhattacharya et al. (2016), the galactic coordinates of this event are quite close to the expected observational fields of the Nancy Grace Roman Space Telescope. Studying and understanding further the stellar population of this field and the distance distribution of the microlensing events is very important for building efficient observational strategies for this space survey. The case of OGLE-2014-BLG-1760 represents a perfect example of the kind of planetary systems we can discover in the Galactic bulge and raises the question of the probability to observe microlensing events with source stars beyond the Galactic bulge.

Acknowledgments

This work was supported by the University of Tasmania through the UTAS Foundation and the endowed Warren Chair in Astronomy and the ANR COLD-WORLDS (ANR-18-CE31-0002) and by NASA through grant NASA-80NSSC18K0274. This research was also supported by the Australian Government through the Australian Research Council Discovery Program (project number 200101909) grant awarded to A.C. and J.P.B. This work was also supported by CNES, focused on Euclid and Roman missions. The Keck Telescope observations and analysis were supported by a NASA Keck PI Data Award, administered by the NASA Exoplanet Science Institute. Data presented herein were obtained at the W. M. Keck Observatory from telescope time allocated to the National Aeronautics and Space Administration through the agency's scientific partnership with the California Institute of Technology and the University of California. The Observatory was made possible by the generous financial support of the W. M. Keck Foundation. The authors wish to recognize and acknowledge the very significant cultural role and reverence that the summit of Maunakea has always had within the indigenous Hawaiian community. We are most fortunate to have the opportunity to conduct observations from this mountain.

ORCID iDs

Natalia E. Rektsini https://orcid.org/0000-0002-1530-4870
Clément Ranc https://orcid.org/0000-0003-2388-4534
Naoki Koshimoto https://orcid.org/0000-0003-2302-9562
Jean-Philippe Beaulieu https://orcid.org/0000-0003-0014-3354
David P. Bennett https://orcid.org/0000-0001-8043-8413
Andrew A. Cole https://orcid.org/0000-0003-0303-3855
Sean K. Terry https://orcid.org/0000-0002-5029-3257
Étienne Bachelet https://orcid.org/0000-0002-6578-5078
Andrzej Udalski https://orcid.org/0000-0001-5207-5619
Joshua W. Blackman https://orcid.org/0000-0001-5860-1157
Aikaterini Vandorou https://orcid.org/0000-0002-9881-4760
Thomas J. Plunkett https://orcid.org/0009-0003-5810-1314
Jean-Baptiste Marquette https://orcid.org/0000-0002-7901-7213

References

Bachelet, E., Hundertmark, M., & Calchi Novati, S. 2024, AJ, 168, 24
Batista, V., Beaulieu, J. P., Bennett, D. P., et al. 2015, ApJ, 808, 170
Beaulieu, J.-P., Bennett, D., Batista, V., et al. 2016, ApJ, 824, 83
Beaulieu, J.-P., Batista, V., Bennett, D., et al. 2018, AJ, 155, 78
Bennett, D. P. 2010, ApJ, 716, 1408
Bennett, D. P. 2014, BAAS, 46, 008
Bennett, D. P., Batista, V., Bond, I. A., et al. 2014, ApJ, 785, 155
Bennett, D. P., Bhattacharya, A., Anderson, J., et al. 2015, ApJ, 808, 169
Bennett, D. P., Bhattacharya, A., Beaulieu, J.-P., et al. 2020, AJ, 159, 68
Bennett, D. P., Bhattacharya, A., Beaulieu, J.-P., et al. 2024, AJ, 168, 15
Bennett, D. P., & Khavinson, D. 2014, PhT, 67, 64
Bennett, D. P., & Rhie, S. H. 1996, ApJ, 472, 660
Bennett, D. P., Udalski, A., Bond, I. A., et al. 2018, AJ, 156, 113
Bensby, T., Adén, D., Melendez, J., et al. 2011, A&A, 533, A134
Bensby, T., Yee, J. C., Feltzing, S., et al. 2013, A&A, 549, A147
Berriman, B. 2024, Keck Data Program ID N027 and Semester 2018A, IPAC, doi:10.26135/KOA3
Bhattacharya, A., Bennett, D. P., Bond, I. A., et al. 2016, AJ, 152, 140
Bhattacharya, A., Bennett, D. P., Beaulieu, J. P., et al. 2021, AJ, 162, 60
Bhattacharya, A., Bennett, D. P., Beaulieu, J. P., et al. 2023, AJ, 165, 206
Bhattacharya, A., Beaulieu, J.-P., Bennett, D. P., et al. 2018, AJ, 156, 289
Blackman, J. W., Beaulieu, J. P., Bennett, D. P., et al. 2021, Natur, 598, 272
Bond, I., Abe, F., Dodd, R., et al. 2001, MNRAS, 327, 868
Bond, I., Bennett, D., Sumi, T., et al. 2017, MNRAS, 469, 2434
Boyajian, T. S., van Belle, G., & von Braun, K. 2014, AJ, 147, 47
Choi, J. Y., Shin, I. G., Han, C., et al. 2012, ApJ, 756, 48
Clarkson, W. I., Sahu, K. C., Anderson, J., et al. 2011, ApJ, 735, 37
Delfosse, X., Forveille, T., Ségransan, D., et al. 2000, A&A, 364, 217
Dong, S., Gould, A., Udalski, A., et al. 2009, ApJ, 695, 970
Drimmel, R., & Spergel, D. N. 2001, ApJ, 556, 181
Gaudi, B. S. 2012, ARA&A, 50, 411
Gaudi, B. S. 2024, BAAS, 56, 2024n4i503p02
Girardi, L., Bertelli, G., Bressan, A., et al. 2002, A&A, 391, 195
Gould, A., Dong, S., Bennett, D. P., et al. 2010a, ApJ, 710, 1800

Gould, A., Dong, S., Gaudi, B. S., et al. 2010b, ApJ, 720, 1073
Gould, A., Udalski, A., An, D., et al. 2006, ApJL, 644, L37
Johnson, S. A., Penny, M., Gaudi, B. S., et al. 2020, AJ, 160, 123
Koshimoto, N., Baba, J., & Bennett, D. P. 2021, ApJ, 917, 78
Koshimoto, N., & Ranc, C. 2022, nkoshimoto/genulens, v1.2, Zenodo, doi:10.5281/zenodo.6869520
Koshimoto, N., Shvartzvald, Y., Bennett, D. P., et al. 2017a, AJ, 154, 3
Koshimoto, N., Udalski, A., Beaulieu, J. P., et al. 2017b, AJ, 153, 1
Li, S. S., Zang, W., Udalski, A., et al. 2019, MNRAS, 488, 3308
Lu, J. R., Gautam, A. K., Chu, D., Terry, S. K., & Do, T. 2021, Keck-DataReductionPipelines/KAI: v1.0.0 Release of KAI, Zenodo, doi:10.5281/zenodo.6677744
Mao, S., & Paczynski, B. 1991, ApJL, 374, L37
Minniti, D., Lucas, P., Emerson, J., et al. 2010, NewA, 15, 433
Nataf, D. M., Gould, A., Fouqué, P., et al. 2013, ApJ, 769, 88
Navarro, M. G., Minniti, D., & Contreras Ramos, R. 2020, ApJ, 902, 35
Nishiyama, S., Tamura, M., Hatano, H., et al. 2009, ApJ, 696, 1407
Penny, M. T., Gaudi, B. S., Kerins, E., et al. 2019, ApJS, 241, 3
Penny, M. T., Henderson, C. B., & Clanton, C. 2016, ApJ, 830, 150
Pecaut, M. J., & Mamajek, E. E. 2013, ApJS, 208, 9
Ranc, C. 2020, Microlensing Observations ANAlysis Tools, v0.1, Zenodo, doi:10.5281/zenodo.4257009
Rektsini, N. E., Batista, V., Ranc, C., et al. 2024, AJ, 167, 145
Shvartzvald, Y., Calchi Novati, S., Gaudi, B. S., et al. 2018, ApJL, 857, L8
Stetson, P. B. 1987, PASP, 99, 191
Street, R. A., Udalski, A., Calchi Novati, S., et al. 2016, ApJ, 819, 93
Sumi, T., Koshimoto, N., Bennett, D. P., et al. 2023, AJ, 166, 108
Surot, F., Valenti, E., Gonzalez, O., et al. 2020, A&A, 644, A140
Suzuki, D., Bennett, D. P., Sumi, T., et al. 2016, ApJ, 833, 145
Terry, S. K., Barry, R. K., Bennett, D. P., et al. 2020, ApJ, 889, 126
Terry, S. K., Beaulieu, J.-P., Bennett, D. P., et al. 2024, AJ, 168, 72
Terry, S. K., Bennett, D. P., Bhattacharya, A., et al. 2022, AJ, 164, 217
Terry, S. K., Bhattacharya, A., Bennett, D. P., et al. 2021, AJ, 161, 54
Tsapras, Y., Street, R., Horne, K., et al. 2009, AN, 330, 4
Tukey, J. 1958, The Annals of Mathematical Statistics, 29, 614
Udalski, A., Szymanski, M., Mao, S., et al. 1994, ApJ, 436
Udalski, A., Szymanski, M. K., Kubiak, M., et al. 2004, AcA, 54, 313
Udalski, A., Yee, J. C., Gould, A., et al. 2015, ApJ, 799, 237
Vandorou, A., Bennett, D. P., Beaulieu, J.-P., et al. 2020, AJ, 160, 121
Yee, J. C., Zang, W., Udalski, A., et al. 2021, AJ, 162, 180